Processes Controlling the Seasonally Varying Emergence of Forced Arctic Longwave Radiation Changes

JONAH K. SHAW[a,b] AND JENNIFER E. KAY[a,b]

[a] *Department of Atmospheric and Oceanic Sciences, University of Colorado Boulder, Boulder, Colorado*
[b] *Cooperative Institute for Research in Environmental Science, University of Colorado Boulder, Boulder, Colorado*

ABSTRACT: Most observed patterns of recent Arctic surface warming and sea ice loss lie outside of unforced internal climate variability. In contrast, human influence on related changes in outgoing longwave radiation has not been assessed. Outgoing longwave radiation captures the flow of thermal energy from the surface through the atmosphere to space, making it an essential indicator of Arctic change. Furthermore, satellites have measured pan-Arctic radiation for two decades while surface temperature observations remain spatially and temporally sparse. Here, two climate model initial-condition large ensembles and satellite observations are used to investigate when and why twenty-first-century Arctic outgoing longwave radiation changes emerge from unforced internal climate variability. Observationally, outgoing longwave radiation changes from 2001 to 2021 are within the range of unforced internal variability for all months except October. The model-predicted timing of Arctic longwave radiation emergence varies throughout the year. Specifically, fall emergence occurs a decade earlier than spring emergence. These large emergence timing differences result from seasonally dependent sea ice loss and surface warming. The atmosphere and clouds then widen these seasonal differences by delaying emergence more in the spring and winter than in the fall. Finally, comparison of the two ensembles shows that more sea ice and a more transparent atmosphere during the melt season led to an earlier emergence of forced longwave radiation changes. Overall, these findings demonstrate that attributing changes in Arctic outgoing longwave radiation to human influence requires understanding the seasonality of both forced change and internal climate variability.

KEYWORDS: Arctic; Infrared radiation; Longwave radiation; Radiation budgets; Satellite observations; Internal variability

1. Introduction

Attributing changes in Earth's climate to human actions remains a challenging and societally relevant task (e.g., National Academies of Sciences, Engineering and Medicine 2016; Knutson et al. 2017; Eyring et al. 2021). Attribution requires both observational records of occurring changes as well as knowledge of the climate's internal variability (variability arising naturally from interactions within the coupled climate system) (Weatherhead et al. 1998). Continuous multidecadal observational records quantify the former, while initial-condition climate model large ensembles have proved an invaluable tool for understanding the latter (Deser et al. 2020). With climate change in the Arctic far outpacing the global mean (e.g., Chylek et al. 2022), evaluating if observed Arctic change has emerged from the background internal climate variability is an especially relevant task. Numerous studies have used observations and large ensembles to investigate the emergence of changes in Arctic surface temperature, sea ice, and precipitation (Gillett et al. 2008; Kay et al. 2011; Barnhart et al. 2016; Fyfe et al. 2013; Kirchmeier-Young et al. 2017; Landrum and Holland 2020; England et al. 2021). In addition to confirming that the rapid pace of observed change is inconsistent with an unforced climate, these studies collectively demonstrate that emergence is occurring at different rates depending on the climate process and the time of the year.

Early coupled global climate models showed that enhanced Arctic warming was driven by local climate processes occurring at the Arctic surface (Manabe and Stouffer 1980). While scientific knowledge of Arctic climate change has matured since then (e.g., Taylor et al. 2022), understanding surface processes remains essential (Screen and Simmonds 2010; Serreze and Barry 2011). Furthermore, surface warming and sea ice loss dominate observed Arctic climate change (Serreze et al. 2009). While previous studies have extensively researched climate change emergence at the Arctic surface, the emergence of changes in the top-of-atmosphere (TOA) energy budget remains relatively unexplored.

Change in TOA radiative energy captures both the drivers of and responses to anthropogenic emissions (e.g., Forster et al. 2021), making it a fundamental indicator of climate change. Observations from NASA's Clouds and the Earth's Radiant Energy System (CERES) mission have measured broadband short- and longwave radiation since 2000, creating a multidecadal record of Earth's radiation budget that is ideal for studies of climate change emergence (Loeb et al. 2018). While emergence studies of TOA radiation have been performed for the global

---

radiation budget (Raghuraman et al. 2021), only the shortwave portion of the Arctic radiation budget has been studied in the context of climate change emergence (e.g., Sledd and L'Ecuyer 2021a,b). Observations of Arctic TOA longwave radiation aid the identification of changing climate processes (Peterson et al. 2019; Boisvert and Stroeve 2015), but there is yet to be a study that examines observed changes over the entire Arctic seasonal cycle and places them in the broader context of internal climate variability.

In this study, we investigate when and why Arctic outgoing longwave radiation will emerge from internal climate variability and thus be attributable to human-caused climate change. We focus on two research questions:

1) When do monthly and annual changes in Arctic longwave radiation emerge from unforced internally generated climate variability, and have any observed changes already emerged?

2) What climate processes drive seasonal differences in the projected emergence of Arctic longwave radiation? Specifically, what are the relative contributions of the Arctic surface, atmosphere, and clouds in controlling the forced trends and internal variability of top-of-atmosphere longwave radiation?

We begin by comparing observed longwave radiation changes with internal variability estimated from the preindustrial control simulation of a coupled climate model. We then use an initial-condition large ensemble from the same climate model to estimate future changes in Arctic longwave radiation and predict future emergence. By separating contributions from the Arctic surface, atmosphere, and clouds, we identify the climate processes both driving and delaying the emergence of longwave radiation changes. Finally, we evaluate the influence of sea ice and clouds by comparing our results with a second climate model ensemble. While we present results for all months of the year, we focus on the Arctic fall and spring when our predictions of emergence are earliest and latest, respectively. We find that variability and forced changes in longwave radiation are closely tied to surface temperatures and sea ice coverage. Additionally, the Arctic atmosphere and clouds delay the emergence of top-of-atmosphere longwave radiation relative to the surface by more in the spring and winter than in the fall.

2. Methods

a. Modeling and observational datasets

To quantify both forced climate change and unforced internal climate variability, we use simulations from the Community Earth System Model Version 1 (CESM1) (Hurrell et al. 2013). CESM1 is a fully coupled global climate model with dynamic atmosphere, ocean, sea ice, and land components. Specifically, we use the CESM1 Large Ensemble (CESM1-LE) (Kay et al. 2015). The CESM1-LE is a single model initial-condition large ensemble consisting of 40 ensemble members with historical forcings applied from 1920 to 2005 and the representative concentration pathway 8.5 forcing ("business-as-usual" emissions scenario) applied from 2006 onward. Individual members of the CESM1-LE exhibit a range of climate responses due to

external forcing and internal climate variability. Averaging these 40 identically forced members of the same model isolates the response to the applied anthropogenic forcing (the forced response). We also use the 1800-yr CESM1-LE preindustrial control simulation with 1850 forcing to quantify internal climate variability in a steady-state climate.

The performance of CESM1 both in and outside of the Arctic has been extensively studied. Critical to the Arctic radiation budget, CESM1 can reproduce the seasonal cycles of sea ice extent and sea ice thickness, as well as the observed record of sea ice loss (Ding et al. 2018; Jahn et al. 2016). Furthermore, the sensitivity of Arctic sea ice extent to observed temperature changes overlaps with observationally derived estimates (Jahn 2018). Critical to studies of climate signal emergence, CESM1 also captures observed variability in Arctic sea ice (Wyburn-Powell et al. 2022). CESM1's representation of the Arctic, however, is not without biases. Specifically, the Arctic surface is colder than observations (Kay et al. 2016; McIlhattan et al. 2020) and there is insufficient liquid-containing cloud cover and longwave cloud radiative effect (English et al. 2014; Kay et al. 2016).

To investigate how differences in the representation of Arctic sea ice and clouds influence emergence, we additionally employ large ensemble simulations from CESM2 (Danabasoglu et al. 2020; Holland et al. 2023, manuscript submitted to *Geosci. Model Dev.*). Changes between CMIP5 and CMIP6 forcings lead to differences in the Arctic climate (Fasullo et al. 2022; Holland et al. 2023, manuscript submitted to *Geosci. Model Dev.*), confounding comparisons between model generations. To remove the influence of inconsistent external forcings, we use simulations of CESM2 with external forcing identical to the CESM1-LE. This ten member ensemble (subsequently referred to as the CESM2-CMIP5) can be directly compared to the CESM1-LE to isolate the influence of model physics on Arctic climate change and climate signal emergence. Compared to CESM1, CESM2 has more liquid containing clouds and an improved representation of downwelling radiation at the Arctic surface (McIlhattan et al. 2020). Conversely, sea ice extent and thickness is reduced in CESM2 relative to CESM1, degrading agreement with observations (DeRepentigny et al. 2020; Kay et al. 2022).

Given the difference in ensemble size between the CESM1-LE and the CESM2-CMIP5, we use bootstrapping to make appropriate comparisons. We resample members of the CESM1-LE to produce bootstrapped ensembles with the same ensemble size as the CESM2-CMIP5. We compare mean values from the CESM2-CMIP5 with 95% confidence intervals estimated from 3000 bootstrapped ensembles of the CESM1-LE. When comparing internal variability between the models, we resample the CESM1-LE preindustrial control run in 500-yr segments to compare appropriately with the CESM2-CMIP5's 500-yr preindustrial control simulation.

In addition to model output, we use up-to-date multidecadal observational records of Arctic change. Most important to this study, we use observed all-sky outgoing longwave radiation (OLR) and absorbed shortwave radiation from the CERES Energy Balanced and Filled (EBAF) Version 4.1 dataset (NASA/LARC/SD/ASDC 2019). These observations can be directly compared with corresponding CESM1 radiation fields. To

additionally understand the importance of clouds and the atmosphere in CESM1, we also use clear-sky outgoing longwave radiation (clear-sky OLR) and surface upwelling longwave radiation fields from model experiments. Finally, we use passive microwave sea ice observations from the NSIDC G02202 v4 data product (Meier et al. 2021) and surface temperature records from the Berkeley Earth Surface Temperature (BEST) dataset (Rohde and Hausfather 2020) to capture Arctic surface change and complement the CERES top-of-atmosphere perspective. All of these observational datasets have monthly temporal resolution, and are interpolated to a common $1° \times 1°$ grid.

b. Defining and estimating the time to emergence of a climate signal

Climate signal emergence occurs when an observed climate change exceeds the background of internal climate variability. With knowledge of internal variability and projections of future change, we can also predict the time to emergence of a climate variable that has not yet emerged in the observational record. Here, we build upon the time-to-emergence methods of Weatherhead et al. (1998), Leroy et al. (2008), and Phojanamongkolkij et al. (2014). These existing methods use a signal-to-noise framework that accounts for the intrinsic internal variability and memory of climate variables. To focus on understanding the climate processes controlling forced change and internal climate variability, we study climate signal emergence in the absence of observational uncertainty.

We use the common definition that a climate signal emerges from internal variability when the measured trend m exceeds two standard deviations of trend uncertainty (Tiao et al. 1990; Weatherhead et al. 1998). Following Leroy et al. (2008) and Phojanamongkolkij et al. (2014), the standard deviation of a climate trend's uncertainty σ_m can be written as

$$\sigma_m = \left(\frac{12dt}{T^3}\sigma_{\text{var}}^2\tau_{\text{var}}\right)^{1/2}, \quad (1)$$

where dt is the time interval, T is the number of evenly spaced points in a measured time series, σ_{var} is the standard deviation of internal climate variability, and τ_{var} is the correlation time of internal climate variability for time scales of one year and longer. The trend uncertainty term σ_m has units of the observed trend (in this case W m^{-2} yr^{-1}), the standard deviation term σ_{var} has units of the climate signal (in this case W m^{-2}), and the correlation τ_{var} has units of the time resolution used (in this case years). The term τ_{var} quantifies the degree of correlation between points in a time series. A value of one indicates that measurements are uncorrelated and contain independent information, while values greater than one indicate correlation between measurements and thus less confidence in a measured trend. For the annual time series evaluated here, $dt = 1$ and is subsequently ignored.

Equation (1) shows that trend uncertainty can be completely characterized by the standard deviation and correlation time of internal variability. While the climate "signal" is simply the measured trend m, the analogous "noise" or net internal variability term is $\sigma_{\text{var}}\tau_{\text{var}}^{1/2}$. We estimate the time to emergence T^*

by setting the magnitude of the observed trend $|m|$ equal to two standard deviations of trend uncertainty and solving for T:

$$T^* = \left(48\frac{\sigma_{\text{var}}^2\tau_{\text{var}}}{|m|^2}\right)^{1/3}. \quad (2)$$

While the signal-to-noise method summarized by Eqs. (1) and (2) provides a useful framework for estimating time to emergence, this method does not diagnose what climate processes cause a signal to emerge. To understand why outgoing longwave radiation emerges earlier or later for different months of the year, we separate the effects of the strength of forced trends and the characteristics of internal variability. We separate each contribution by comparing each month to an "average month," where the average month has the mean properties of all months of the year. The "average month" is distinct from the annual average because forced trends and internal variability characteristics are calculated before averaging across all months. The time to emergence of the average month is then given by

$$T_{\text{avg}}^* = \left(48\frac{\overline{\sigma_{\text{var}}}^2\overline{\tau_{\text{var}}}}{\overline{|m|}^2}\right)^{1/3}, \quad (3)$$

where overbars indicate an average taken over all months of the year. The internal variability terms τ_{var} and σ_{var} are constant, but the strength of the forced trend m varies in time. Consequently, we calculate $|m|$ at the mean time of emergence for each month to ensure consistency with monthly estimates of time to emergence.

The time to emergence for any month can then be written as the time to emergence of the average month scaled by terms describing how the strength of the forced trends and internal variability differ from the "average month":

$$T^* = T_{\text{avg}}^*\left(\frac{\tau_{\text{var}}}{\overline{\tau_{\text{var}}}}\right)^{1/3}\left(\frac{\sigma_{\text{var}}}{\overline{\sigma_{\text{var}}}}\right)^{2/3}\left(\frac{\overline{|m|}}{|m|}\right)^{2/3}. \quad (4)$$

The last three terms in Eq. (4) quantify the relative importance of the correlation time of internal variability, the standard deviation of internal variability, and the strength of forced trends to differences in climate signal emergence between months of the year, respectively. Values greater than one indicate that emergence is delayed relative to the average month while values less than one indicate that emergence is accelerated relative to the average month.

c. Improving estimates of climate signal emergence with climate model large ensembles

The previously described signal-to-noise method [Eqs. (1) and (2)] was developed with observational time series in mind. This method has advantages that make it an excellent tool to aid satellite mission design: it can be expanded to account for additional sources of uncertainty and is well-suited for predicting emergence using a single incomplete observational time series (Weatherhead et al. 1998; Leroy et al. 2008; Wielicki et al. 2013). The signal-to-noise method, however, does not consider how information about climate variability and future climate change can be used to improve estimates of climate signal
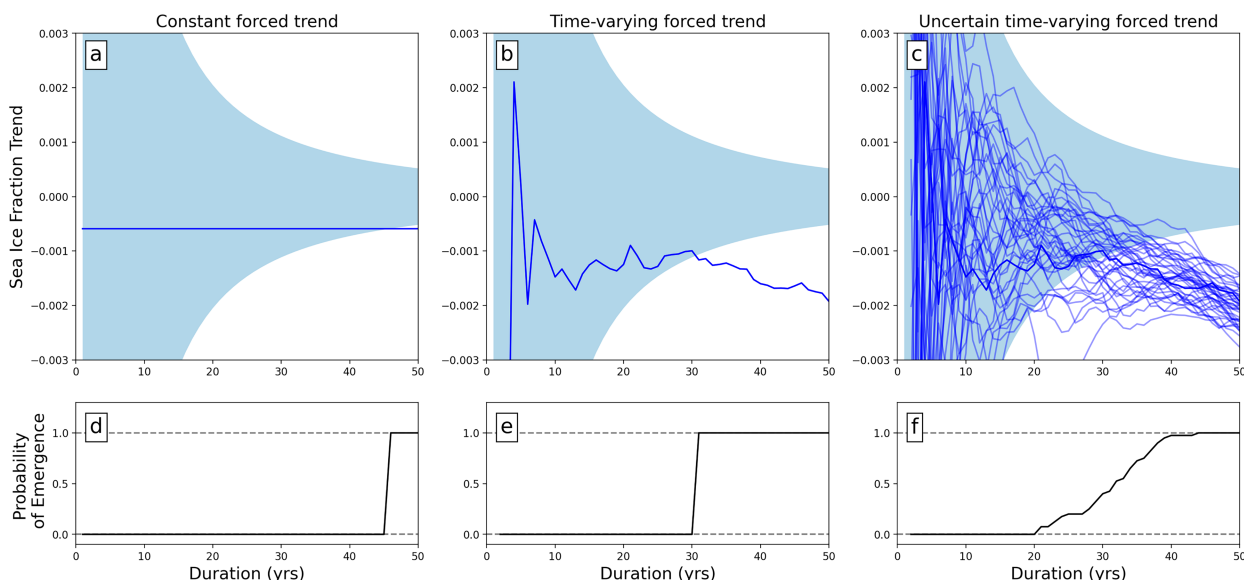
FIG. 1. Predicting climate signal detection aided by climate model simulations. Changes in central Arctic (70°–90°) December sea ice fraction data are used as an example. (a) A constant forced trend (solid line) compared to two standard deviations of internal climate variability (shaded region), (b) a time-varying forced trend from a single climate model simulation (solid line) compared to two standard deviations of internal climate variability (shaded region), and (c) 40 time-varying forced trends from a climate model large ensemble (solid lines) compared to two standard deviations of internal climate variability (shaded region). (d)–(f) The probability of climate signal emergence corresponding to the forced trends assumed in (a)–(c), respectively. Time-varying trends are taken from the CESM1 Large Ensemble, and the background of internal climate variability is taken from the CESM1 preindustrial control simulation and calculated using Eq. (1).

emergence. Indeed, the signal-to-noise method ignores that 1) trends may vary in time due to nonlinearities in both forcings or feedbacks, 2) trends may have large reasonable ranges resulting from internal climate variability, and 3) climate variability (both correlation time and standard deviation) may differ between the preindustrial and modern climate states. In particular, ignoring the range of possible forced trends avoids acknowledging that time to emergence is inherently uncertain due to internally generated climate variability.

Ensemble climate model simulations can be used to overcome the limitations of the signal-to-noise method. First, individual model ensemble members can project future climate changes (Fig. 1b). These simulations account for future changes in forced trends that cannot be inferred from observations (Fig. 1a). Second, initial condition large ensembles enable the separation of forced and unforced climate changes. Knowledge of the forced response removes uncertainty due to internal variability from the predicted time to emergence (Fig. 1c). Additionally, knowledge of unforced climate changes allows time to emergence to be described probabilistically rather than as a single time (Figs. 1d–f).

Long preindustrial control model simulations also provide a valuable tool for time-to-emergence studies. Simply put, these simulations allow one to calculate the background of internal variability from an unforced climate rather than attempting to disentangle forced and unforced climate change. Furthermore, we can use preindustrial control simulations to study the influence of changing internal variability on predictions of emergence.

Informed by the above analysis (Fig. 1) and previous methods, we employ the following approach for estimating time to emergence. 1) We compute monthly and annual-averaged time series of Arctic OLR as area-weighted means over the Arctic (70°–90°N) for observed and modeled fields. Our comparisons of twenty-first-century time series (CERES observations and the CESM1-LE) begin in 2001, the first complete year of the CERES record. 2) We calculate the standard deviation and correlation time of internal variability using the CESM1 preindustrial control simulation. When calculating the correlation time, we use the method of Weatherhead et al. (1998), which calculates the correlation time using the lag one value of the autocorrelation function. Compared to the method of Leroy et al. (2008), Weatherhead et al. (1998) leads to lower error in estimates of unforced trend uncertainty (Fig. S1 in the online supplemental material). 3) We use our estimated standard deviation and correlation time to calculate the background of internal variability [σ_m in Eq. (1)]. 4) We calculate emergence by combining internal variability with observed and modeled OLR time series using Eq. (2). We use an approach similar to Feldman et al. (2011) and Sledd and L'Ecuyer (2021a) to account for the time dependence of forced trends. Namely, a trend in the climate signal of interest is recalculated after each year is added to the time series. Then, each trend is compared to trend uncertainty resulting from internal variability, and emergence occurs when the trend exceeds two standard deviations of this trend uncertainty for the last time. We repeat this process for each member of the large ensemble to generate a distribution of emergence times due to internal climate variability. 5) Finally, we bootstrap this
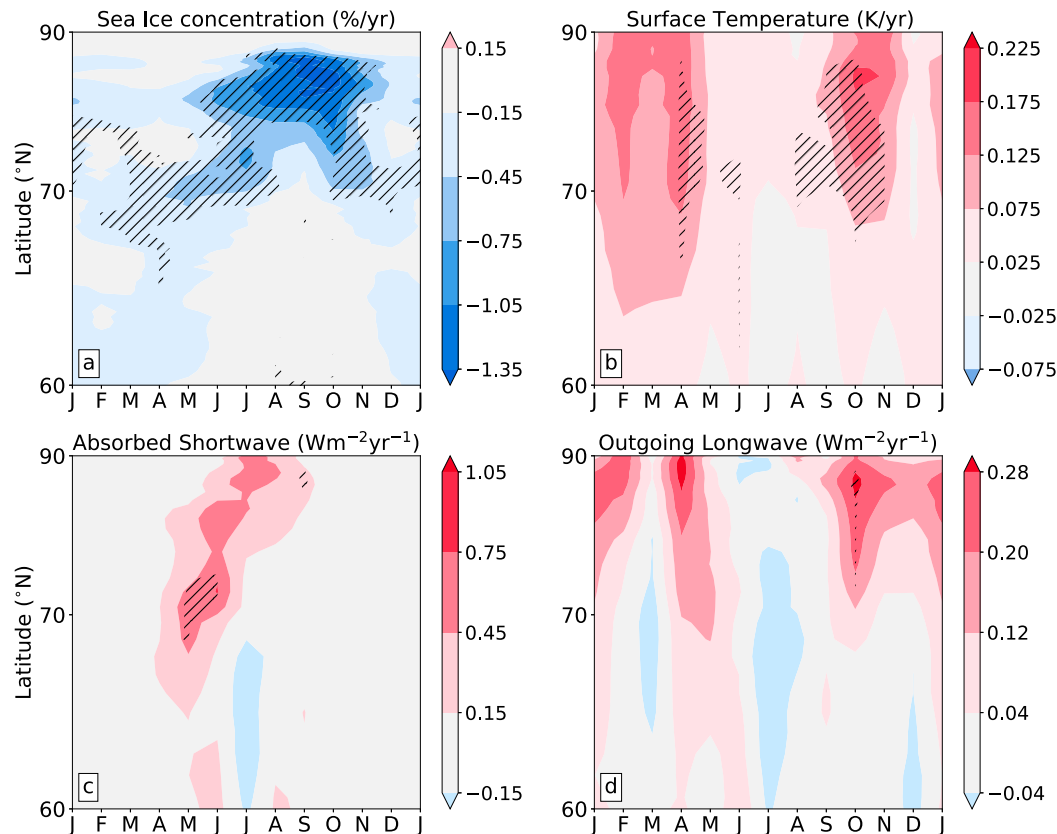
FIG. 2. Observed Arctic trends over the period 2001–21: (a) sea ice concentration from the National Snow and Ice Date Center G02202 data product (Meier et al. 2021), (b) surface temperature from the Berkeley Earth Surface Temperatures gridded data product (Rohde and Hausfather 2020), (c) absorbed shortwave radiation from Clouds and the Earth's Radiant Energy System (CERES) (TOA v4.1) (NASA/LARC/SD/ASDC 2019), and (d) all-sky outgoing longwave radiation from CERES (TOA v4.1) (NASA/LARC/SD/ASDC 2019). Stippling indicates trend confidence > 99% calculated using a Student's *t* test.

distribution 3000 times to estimate confidence intervals on time to emergence.

3. Results

a. Observed and modeled changes in Arctic climate (2001–21)

For broad context, we begin by presenting observations of multiple Arctic climate variables that are all available over the time period 2001–21. These observations show Arctic sea ice loss, surface warming, and corresponding changes in top-of-atmosphere radiation (Fig. 2). In recent decades, Arctic sea ice extent decreases occurred at the seasonally varying sea ice margin (Fig. 2a). Each year, seasonal ice loss began at the southerly sea ice edge in March and April and moved northward following the ice edge retreat. The greatest and most northerly sea ice loss of all months occurred in September. During October and November, the location of the greatest ice loss shifted back South following the ice edge. Surface temperature changes (Fig. 2b) show the greatest warming in

the fall and spring and only modest warming in the summer. In contrast to surface temperature, increases in absorbed shortwave radiation (Fig. 2c) were greatest during peak insolation in June and July. Shortwave changes shifted to more northerly latitudes from May to July, following the northward retreat of the sea ice edge. Finally, OLR (Fig. 2d) increased poleward of 70°N from September through February. Notably, OLR increases coincided meridionally and seasonally with surface temperature increases.

Having documented recent observed changes, we next assess how these observed changes compare to the forced response from the CESM1-LE. Overall, forced trends (Fig. 3) strongly resemble the observed trends (Fig. 2), demonstrating the human fingerprint on Arctic climate change. Indeed, observed Arctic change bears a strong spatial and seasonal resemblance to the forced response. Like observations, the forced response shows sea ice loss following the sea ice edge during retreat and advance (Fig. 3a). Corresponding increases in absorbed shortwave radiation (Fig. 3c) resemble patterns of sea ice loss during the bright summer months. Also similar to observations, large surface warming in the
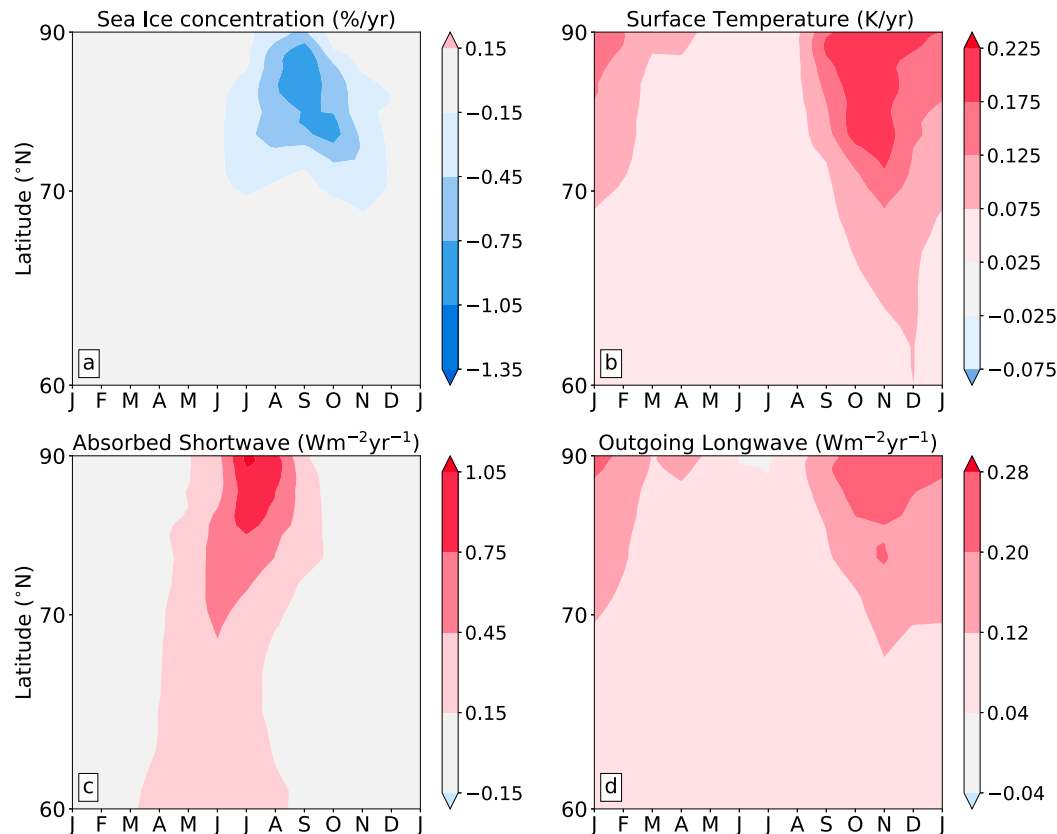
FIG. 3. Arctic trends over the period 2001–21 from the CESM1-LE forced response: (a) sea ice concentration, (b) surface temperature, (c) absorbed shortwave radiation, and (d) all-sky outgoing longwave radiation.

fall (Fig. 3b) is associated with increases in outgoing longwave radiation (Fig. 3d). A notable exception is observed spring warming, which is absent from the forced response (Fig. 3b).

In addition to providing an estimate of the forced response, we also use the CESM1-LE to quantify internal climate variability. The standard deviation in CESM1-LE Arctic trends (Figs. 4a–d) shows where internal climate variability contributes uncertainty to simulated Arctic climate change. Interestingly, this internal variability uncertainty resembles the magnitude of the forced trends across all variables. In other words, the rate of forced change is generally faster when unforced internal variability is large. Internal variability in April and May OLR changes (Fig. 4d), however, is disproportionately large relative to forced OLR trends (Fig. 3d). This enhanced OLR variability during the Arctic spring suggests that observed OLR increases (Fig. 2d) have large contributions from internal climate variability.

The ratio of the forced response (signal) to the trend standard deviation (noise) provides a simple estimate of trend significance (Figs. 4e–h). All variables show distinct spatial and temporal features in their signal-to-noise ratios. In the sea ice, surface temperature, and OLR fields, signal-to-noise ratios are larger in the fall months than in other parts of the year. This seasonality suggests that forced changes during the fall

are more significant than other months. Compared to sea ice and surface temperature, however, the signal-to-noise ratio for OLR is smaller. From this comparison, we expect that the emergence of OLR changes will lag that of surface warming and sea ice loss.

We next present changes in Arctic OLR (Fig. 5) to compare observations with the CESM1-LE. Overall, Fig. 5 shows that Arctic OLR changes vary seasonally, but are also subject to large uncertainty from internal variability. Average monthly OLR changes from the CESM1-LE are largest from October through January and smallest during June and July (Fig. 5a). Despite this seasonal behavior present in the forced response, confidence intervals on the forced changes show that internal variability makes the magnitude and even sign of OLR changes from any single ensemble member uncertain. Observationally, OLR changes from CERES lie within the 95% confidence interval of the large ensemble for all months except August. The distinct seasonal maximum and minimum seen in the modeled forced response, however, are obscured by internal climate variability in CERES observations.

Finally, we compare observed OLR changes from CERES with unforced changes in the preindustrial control simulation (Fig. 5b) to investigate if observed change can be distinguished from internal climate variability. Only observed OLR changes
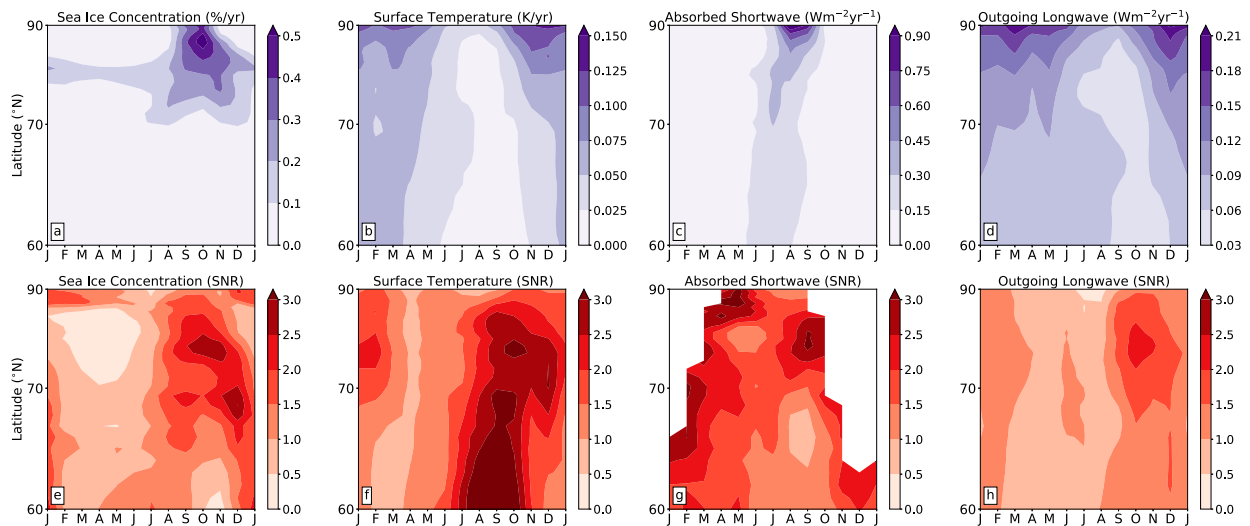
FIG. 4. Arctic OLR trend standard deviations and signal-to-noise ratios (SNRs) over the period 2001–21 from members of the CESM1-LE. (a)–(d) The standard deviation of sea ice concentration, surface temperature, absorbed shortwave radiation, and all-sky outgoing longwave radiation trends from members of the CESM1-LE ($N = 40$), respectively. (e)–(h) As in (a)–(d), but for the SNR of Arctic trends from the CESM1-LE forced response (Fig. 3) relative to trend standard deviations. In (g), latitudes with monthly mean solar insolation less than 10 W m^{-2} are masked.

in October lie outside of the confidence interval on unforced trends, indicating that most 2001–21 observed monthly OLR changes are not distinct from unforced internal variability. Our definition of emergence requires that a trend leaves the range of unforced variability and remains outside of that range. Because the CERES October trend sits just outside of internal variability and may re-enter with additional years of observations, we state only that the trend is outside of internal variability.

b. Quantifying Arctic outgoing longwave radiation time to emergence

Having presented OLR change and internal variability separately (Figs. 2–5), we now combine forced changes and variability to predict the emergence of OLR trends for an observational record beginning in 2001 (Fig. 6). Changes in annual mean OLR emerge after 20 years on average, with a 95% confidence interval from 12 to 30 years. Comparing time to emergence for individual months shows a seasonal cycle
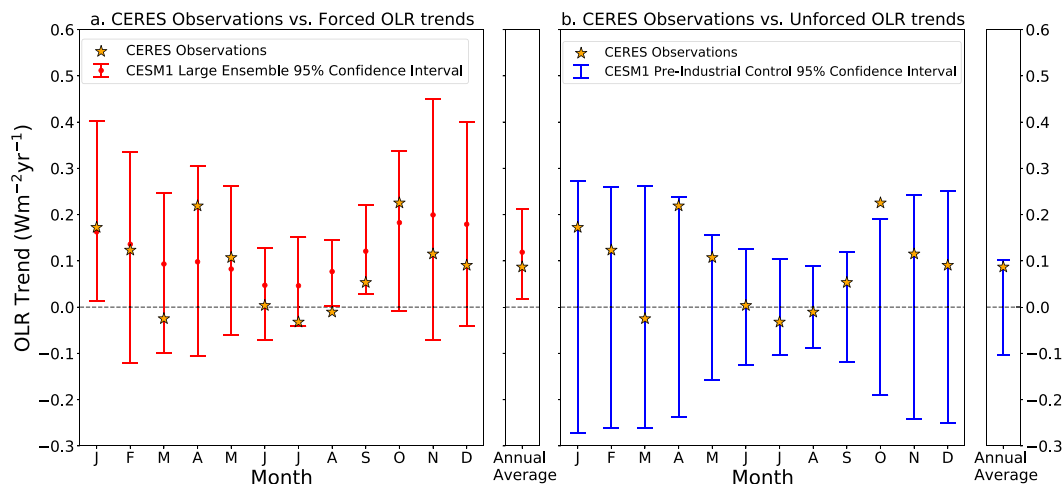

FIG. 5. Monthly and annual trends in all-sky Arctic outgoing longwave radiation (2001–21). (a) Red markers show mean outgoing longwave radiation trends from the CESM1-LE. Vertical lines span 95% confidence interval on single-member trends calculated using bootstrapping. Stars show observed trends from CERES over the same period. (b) Blue lines span a 95% confidence interval on single-member 21-yr unforced trends from the CESM1-LE pre-industrial control simulation calculated using Eq. (1). Stars are as in (a).
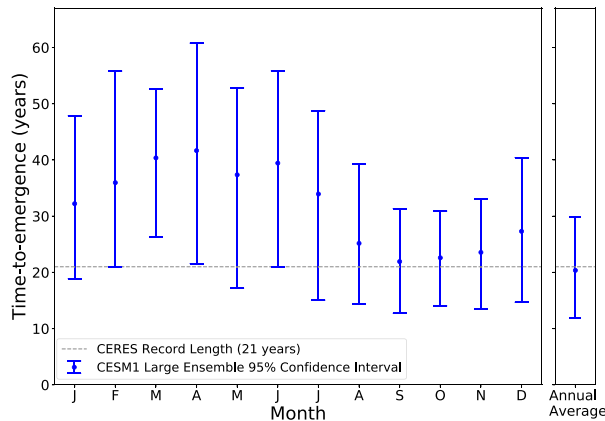
FIG. 6. Monthly and annual time to emergence of all-sky Arctic outgoing longwave radiation for members of the CESM1 Large Ensemble. Error bars span a bootstrapped 95% confidence interval on estimated time to emergence. The dashed gray line indicates the current length of the CERES observational record.

with earlier emergence in the fall and later emergence in the spring. In particular, the mean time-to emergence in September (22 years, 95% confidence interval 13–31 years) occurs two decades before the mean time to emergence in April (42 years, 95% confidence interval 22–61 years). While simulated OLR changes from some members of the CESM1-LE do emerge during the period of the current CERES record (2001–21), observed changes largely remain within internal variability (Fig. 5).

Because OLR emergence varies spatially, we present Arctic maps of time to emergence in Fig. 7. Spatial patterns of time to emergence show that even for a single month, some locations emerge as much 50 years before others. In November, for example, the average time to emergence at latitudes poleward of 80°N is generally 20–30 years while the time to emergence in the Barents and Greenland Seas is greater than 70 years. These large differences in the spatial time to emergence indicate that the climate processes that mediate OLR trends and variability are not constant over the Arctic.

Next, we compare the spatial time to emergence with that of the area-weighted Arctic (70°–90°N). This comparison enables us to understand how spatial averaging influences OLR emergence. In general, the spatial time to emergence is longer than the Arctic average. This occurs because Arctic averaging reduces internal climate variability and thus trend uncertainty. However, in some months and regions the spatial time to emergence is similar to or even less than the Arctic average (e.g., latitudes poleward of 80°N in October–December). In these locations, the rapid pace of local change outweighs the reduction in trend uncertainty from spatial averaging.

The annual cycle of emergence shown in Fig. 6 differs from corresponding annual cycle in the forced trends (Fig. 5). For example, the largest forced trends occur in November, but the earliest emergence occurs two months before in September. In other words, the monthly pattern of forced trends alone cannot explain the monthly pattern of emergence. This mismatch

between forced trends and time to emergence leads us to next investigate monthly patterns of internal climate variability.

To understand seasonal variations in OLR internal variability, we next compare monthly values of the standard deviation and correlation time of Arctic OLR (Fig. 8). Monthly OLR standard deviations are smallest in the boreal summer and greatest in the winter. In the summer, surface emission temperatures are tied to the melting point of water due to latent heat changes from sea ice melt. Even in the absence of sea ice, the large thermal reservoir of the open ocean moderates surface temperatures and OLR. Conversely, relatively large winter OLR variability coincides with an ice-covered Arctic surface with relatively low heat capacity. Most months have correlation times near one (Fig. 8b), indicating little memory at interannual and longer time scales. Performing the annual average removes monthly scale variability and reduces the standard deviation of internal variability (Fig. 8a). Lower frequency variability increases in the annual average, however, increasing the correlation time (Fig. 8b). Correlation times are greater than one in September and October because OLR during these months is a response to shortwave energy absorbed over the entire melt season, naturally averaging over nearly half of the year.

Having examined monthly and annual differences in internal variability and forced trends, we now quantify how these differences delay and accelerate emergence. Equation (4) allows us to distinguish the relative importance of internal variability and forced trends throughout the year (Fig. 9). Monthly differences in correlation time generally have a relatively small (<10%) influence on time to emergence (blue bars). The correlation time is of secondary importance to emergence even in September and October when the correlation time is anomalously large. Monthly OLR standard deviations (orange bars) accelerate emergence in the summer and delay it in the fall and winter. Compared to the standard deviation, differences in forced trends (green bars) have a similar magnitude effect but different timing. Specifically, the seasonality of forced trends delays summer emergence and accelerates fall and winter emergence. As a result, the effects of internal variability magnitude and forced trend strength on time to emergence oppose each other for most of the year, similar to how the forced trend strength and standard deviation in Figs. 3 and 4 resemble each other. Interestingly, the earliest (September) and latest (April) months to emerge occur in the shoulder seasons when trend strength and uncertainty do not oppose each other.

Studying OLR emergence using monthly resolution time series shows the importance of seasonal Arctic climate process. Choosing a temporal resolution determines the relevant time scales of both trends and variability. For example, averaging annually reduces variability while also removing the seasonality of forced change. Figure S2 compares OLR time to emergence at temporal resolutions from one day to one year. We find that monthly averages capture the seasonality of forced change while reducing variability relative to higher resolution time series. On the other hand, annually averaged OLR emerges earliest on average, but does not resolve the seasonal features of the Arctic climate system.
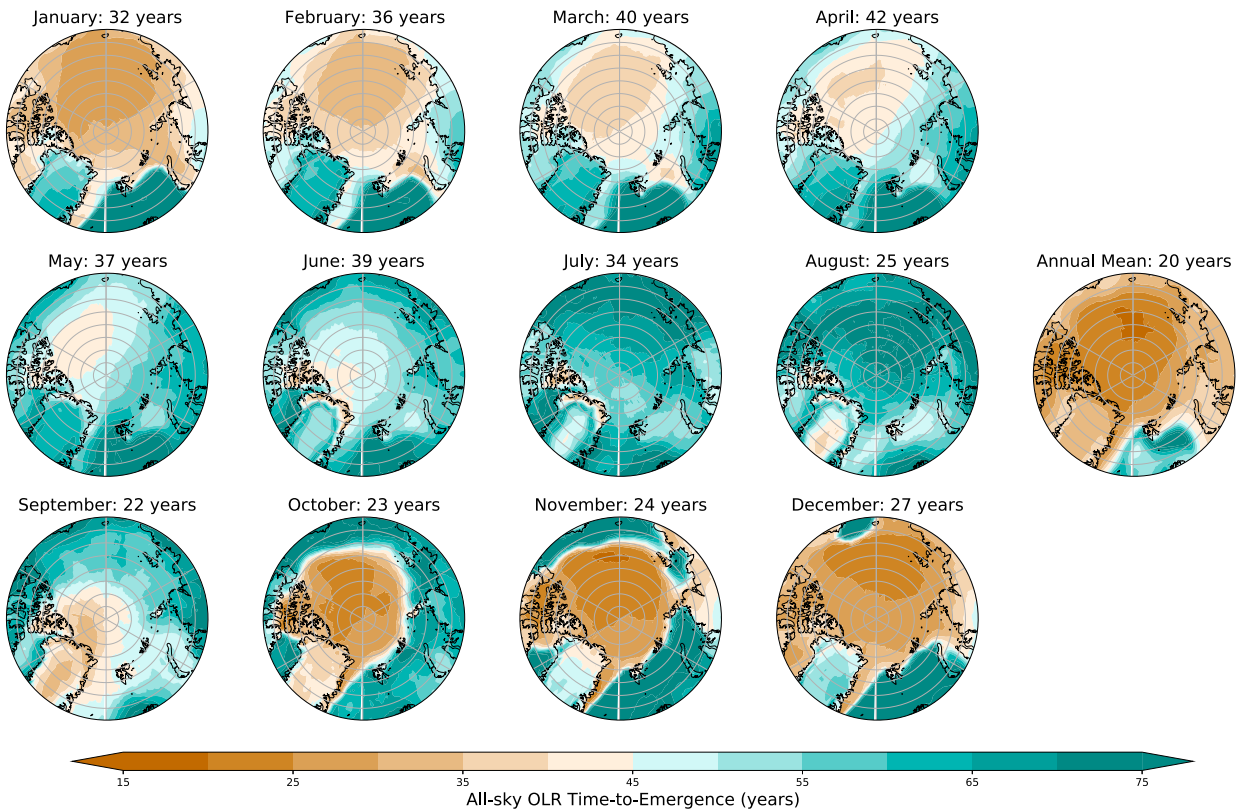
FIG. 7. Spatial maps of the monthly and annual mean time to emergence of all-sky Arctic outgoing longwave radiation (OLR). Panels show the CESM1-LE ensemble mean time to emergence for time series beginning in 2001. The time to emergence of the area-weighted Arctic (70°–90°N) average OLR from Fig. 6 is reported in the title of each plot.

c. Surface and top-of-atmosphere longwave radiation changes

We next separate the influence of the Arctic surface, atmosphere, and clouds on OLR emergence. Surface upwelling longwave radiation, clear-sky OLR, and OLR from the CESM1-LE, respectively, represent the longwave radiation from the surface alone, the surface and clear-sky atmosphere, and the surface and all-sky atmosphere. Comparing changes in these radiation variables (Fig. 10) illustrates how the atmosphere and clouds
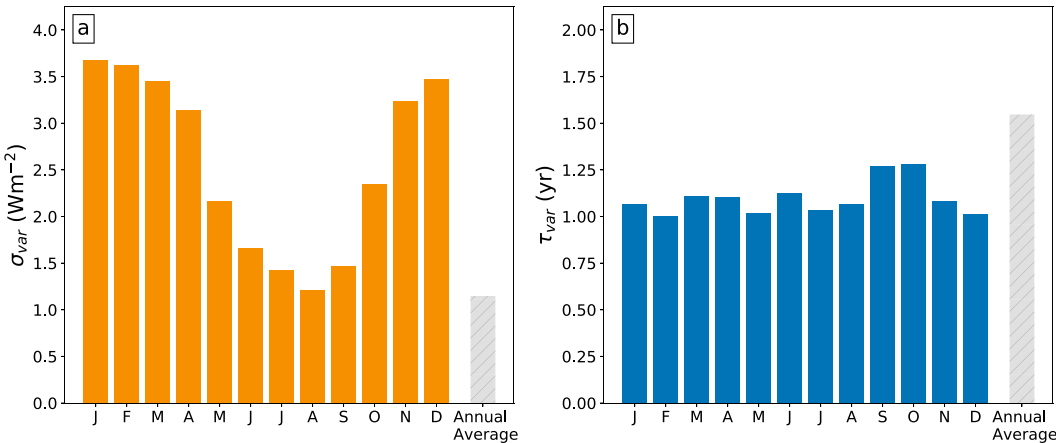

FIG. 8. Preindustrial internal variability in Arctic outgoing longwave radiation: (a) standard deviation (σ_{var}) and (b) correlation time (τ_{var}). Values are calculated using years 400–2200 of the CESM1 1850 preindustrial control simulation.
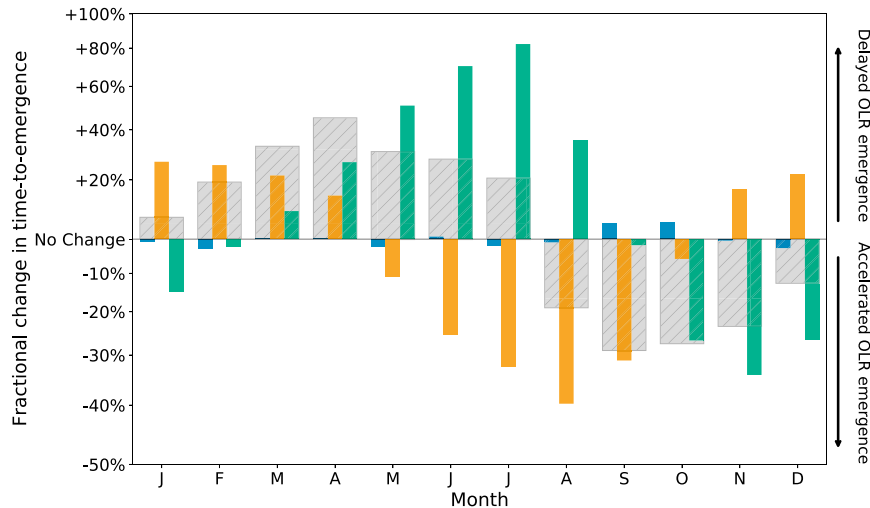
FIG. 9. Monthly differences in emergence time (gray) decomposed into contributions from correlation time τ_{var} (blue), standard deviation σ_{var} (orange), and trend m_{est} (green). Values are calculated from Eq. (4) using the CESM1 Large Ensemble and years 400–2200 of the CESM1 1850 preindustrial control simulation.

damp the signal of surface-driven OLR changes. Increases in surface upwelling longwave radiation are always larger than increases in OLR and clear-sky OLR, indicating a strengthening greenhouse effect. Specifically, the trend in annually averaged upwelling surface longwave radiation increases by 32% while the trend in annually averaged OLR increases by only 7% (Fig. 10b). These greater increases in surface upwelling longwave radiation are consistent with surface-dominated Arctic warming. Expressed in the context of radiative forcings and feedbacks, the negative feedback from surface warming via the Planck effect is opposed at the TOA by both greenhouse gas forcing and positive feedbacks active in the Arctic. The same positive feedback

processes that enhance Arctic warming also delay OLR emergence.

Temporally, differences between OLR and surface upwelling longwave radiation trends increase between the period of the current CERES record (2001–21, Fig. 10a) and the first half of the twenty-first century (2001–50, Fig. 10b). To further show how the greenhouse effect evolves in time, we additionally include time series of the normalized all-sky and clear-sky greenhouse effect in Fig. S3. All months show an increasing greenhouse effect, but changes in November, December, and January are the largest. Overall, Fig. 10 and Fig. S3 show that increases in surface upwelling longwave radiation are damped at the TOA by an increasingly opaque atmosphere.
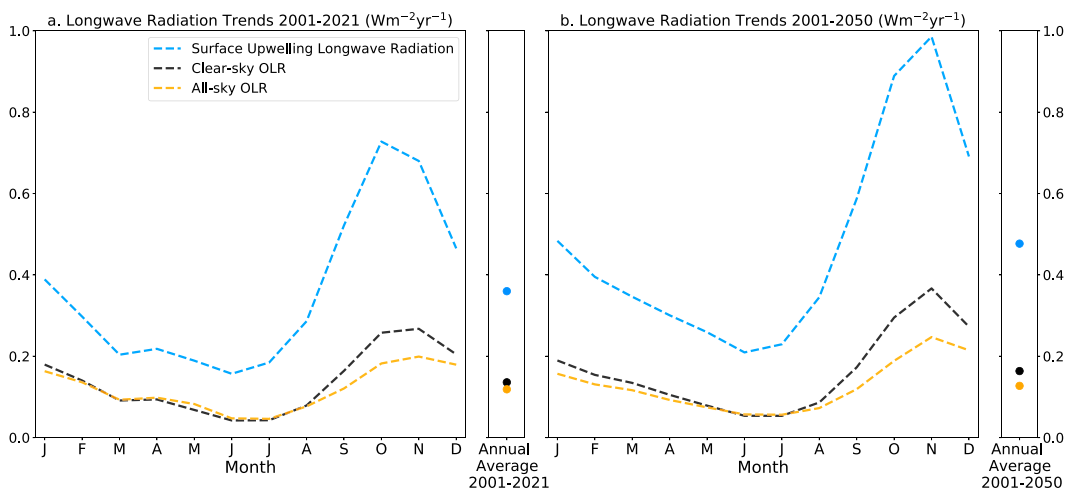

FIG. 10. Surface and top-of-atmosphere longwave radiation (OLR) trends from the CESM1 Large Ensemble forced response: (a) 2001–21 and (b) 2001–50. Blue lines show surface upwelling longwave radiation trends. Black lines show clear-sky OLR trends. Yellow lines show all-sky OLR trends.
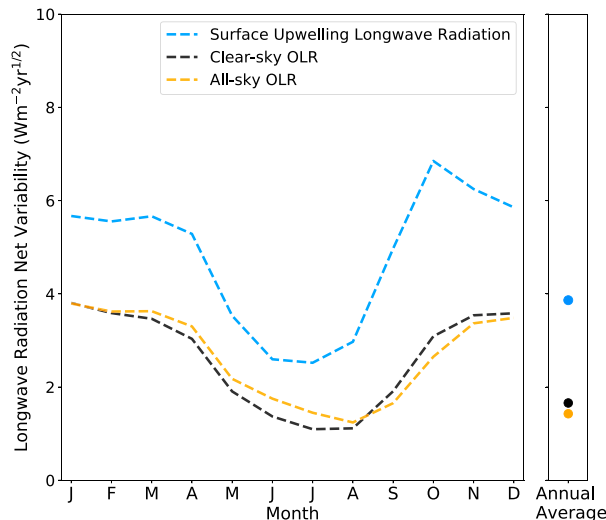
FIG. 11. Monthly and annual longwave radiation net variability estimated from the CESM1 preindustrial control simulation. Blue lines show surface upwelling longwave radiation variability. Black lines show clear-sky OLR variability. Yellow lines show all-sky OLR variability.

To complete our understanding of how the atmosphere and clouds influence OLR emergence, we now examine internal variability for all three radiation fields. Having previously shown that the correlation time of internal variability explains little of the monthly differences in emergence (Fig. 9), we combine the standard deviation and correlation time to present the net internal variability in Fig. 11. Net internal variability is lowest in the summer and greatest in the Arctic fall and winter for all OLR fields. This seasonal pattern resembles the standard deviation of OLR (Fig. 8) and confirms that the standard deviation term largely determines the annual cycle of OLR internal variability. Comparing longwave radiation fields, the variability of clear-sky OLR and all-sky OLR is less than surface upwelling longwave radiation for all months. The atmosphere damps variability in surface upwelling longwave radiation for all months, preserving the seasonal cycle of internal variability. Quantitatively, however, the greatest fractional reductions in the variability of all-sky OLR relative to surface upwelling longwave radiation occur from August through November. Clouds damp variability more than the atmosphere alone during these months, while slightly increasing variability during the early summer. Overall, the atmosphere and clouds' damping effect on OLR variability is greatest in the late summer and fall when the atmosphere is moist and opaque.

Combining forced trends (Fig. 10) and internal variability (Fig. 11), we present the time to emergence of changes in OLR, clear-sky OLR, and surface upwelling longwave radiation from the CESM1-LE (Fig. 12). All three variables show emergence occurring earliest in the fall and latest in the spring. Additionally, surface longwave radiation emerges before the top-of-atmosphere longwave radiation for all months, indicating that the Arctic atmosphere and clouds always delay
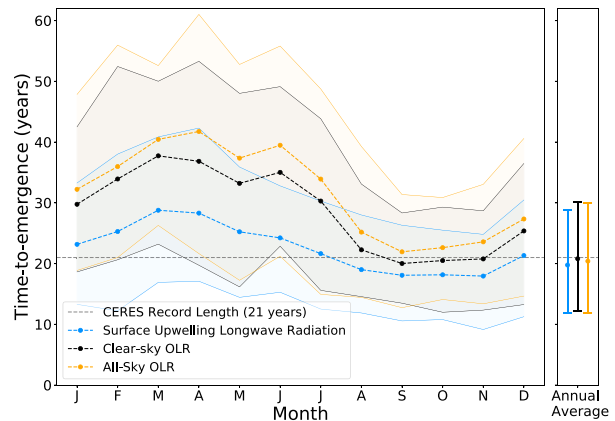

FIG. 12. Monthly and annual time to emergence of changes in longwave radiation variables for members of the CESM1 Large Ensemble. Blue lines show surface upwelling longwave radiation time to emergence. Black lines show clear-sky OLR emergence. Yellow lines show all-sky OLR emergence, reproduced from Fig. 6. Shaded regions and error bars span a 95% confidence interval on estimated time to emergence. The dashed gray line indicates the current length of the CERES observational record. Time to emergence is calculated with respect to time series beginning in 2001.

emergence. How long the atmosphere and clouds delay emergence by, however, varies by month. From December through July, the Arctic atmosphere and clouds delay emergence by up to 15 years relative to surface upwelling longwave radiation. From August through December, on the other hand, emergence is only slightly delayed. By delaying OLR emergence most in the winter and spring, the atmosphere and clouds enhance monthly differences in the time to emergence of surface upwelling longwave radiation.

The atmosphere and clouds enhance these monthly differences by unequally damping variability in surface upwelling longwave radiation. At the surface, variability in upwelling longwave radiation is greater in the fall than in the spring (Fig. 11). At the TOA, however, all-sky OLR variability is less in the fall than in the spring. With less variability at the TOA relative to the spring, fall changes emerge earlier and seasonal differences are widened.

d. Influence of changing outgoing longwave radiation variability on time to emergence

So far, we have neglected the influence of changing OLR variability on emergence. Here, we assess if this simplification is justified. We first note that twenty-first-century OLR variability does not affect the forced response and thus the mean time to emergence. If OLR variability changes, however, so will the uncertainty in projected change and the range of possible emergence times. We investigate if the uncertainty in twenty-first-century OLR changes differs from uncertainty in unforced preindustrial OLR changes (Fig. 13). For all months of the year, the uncertainty in twenty-first-century OLR trends is not statistically different from the preindustrial climate. While some months like October do show a change in
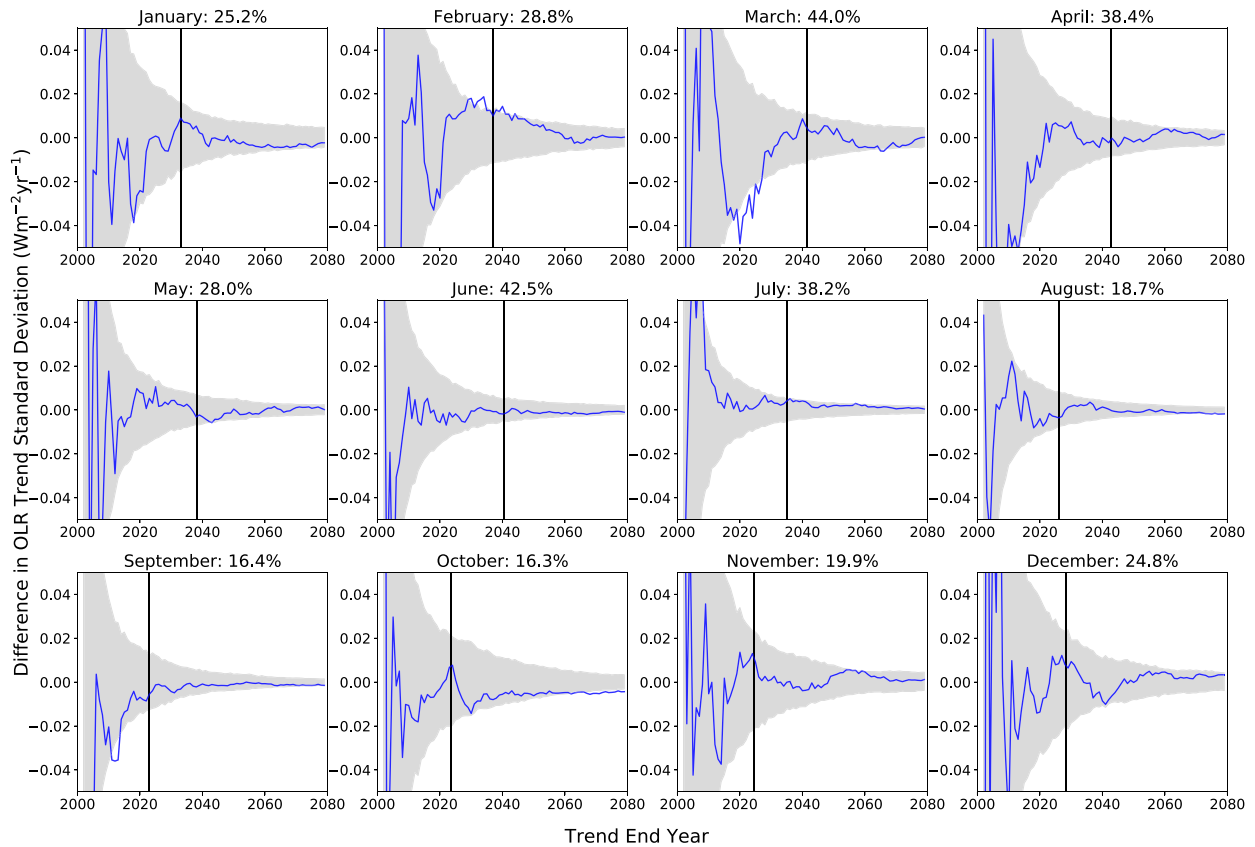
FIG. 13. Difference between forced and unforced OLR trend standard deviations. Blue lines show the difference between the standard deviation of forced trends beginning in 2001 from the CESM1-LE ($N = 40$) and the average standard deviation of trends of the same length from the CESM1-LE preindustrial control simulation. The gray shaded region indicates a 95% confidence interval on unforced trend standard deviations also calculated from the CESM1-LE preindustrial control simulation. Vertical bars indicate the mean time to emergence of outgoing longwave radiation. Positive (negative) values on the y axis indicate more (less) trend variability than the preindustrial Arctic. The 95% confidence interval of mean 21-yr trends from a 40-member ensemble is expressed as a percentage of the CESM1-LE mean 2001–21 OLR trend in the title of each subplot.

trend variability, these changes occur decades after OLR emergence. Despite significant changes in the variability of OLR itself (Fig. S4), emergence is unaffected. Overall, Fig. 13 shows that changes in twenty-first-century variability are too small and come too late to modify OLR time to emergence. Thus, neglecting the influence of changing OLR variability is an acceptable assumption for this study.

Figure 13 also shows that ensemble-derived estimates of variability and the forced response are made uncertain due to the relatively small ensemble size. We have already shown the influence of nonstationarity in variability on emergence timing is small. Thus, we use the preindustrial control simulation to quantify the influence of ensemble size on ensemble mean OLR trends (the forced response). Comparing this uncertainty to the CESM1-LE mean monthly OLR trends (Fig. 13 subpanel titles) indicates that even with 40 ensemble members, fractional uncertainty in the CESM1-LE forced response is 16%–44% depending on the month of the year. This uncertainty in the forced response can only be reduced by increasing the ensemble size. However, we avoid corresponding

uncertainty in internal climate variability by using preindustrial control simulations to estimate the background of internal climate variability. In sum, Fig. 13 demonstrates that ensemble-based estimates of both a model's forced response and internal variability are uncertain. Internal variability should be estimated from long preindustrial control simulations whenever possible.

e. Influence of sea ice and clouds on OLR emergence

We next investigate how the differing representations of clouds and sea ice in the CESM1-LE and the CESM2-CMIP5 influence the time to emergence of OLR. Comparing the mean OLR time to emergence from the CESM2-CMIP5 with the CESM1-LE (Fig. 14), we find that fall and early winter months (September–February) emerge later in the CESM2-CMIP5 than in the CESM1-LE. Outside of these months, OLR emergence in the CESM2-CMIP5 is not statistically different from the CESM1-LE. Spring months still emerge later than fall months in the CESM2-CMIP5, but the large seasonal differences present in the CESM1-LE are notably reduced.
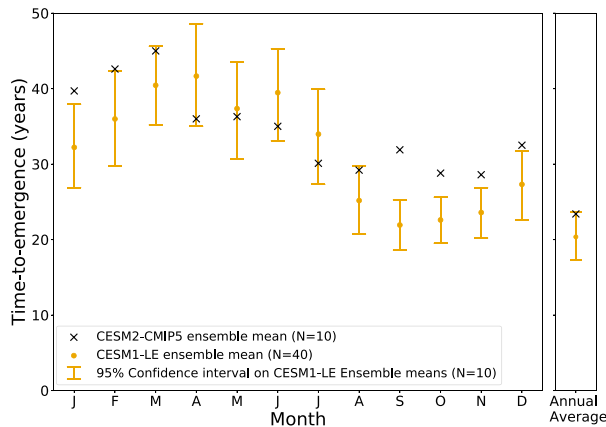
FIG. 14. Monthly and annual time to emergence of all-sky Arctic outgoing longwave radiation (OLR) for CESM2-CMIP5 simulations. The mean time to emergence of OLR from 10 simulations of CESM2 with CMIP5 forcing (CESM2-CMIP5) is compared with the CESM1-LE. Black crosses show the mean time to emergence of the CESM2-CMIP5 simulations. Yellow markers and error bars, respectively, show the mean time to emergence of the CESM1-LE and a 95% confidence interval obtained by bootstrapping with samples of 10 for comparison with the CESM2-CMIP5 simulations.

To understand why fall OLR in the CESM2-CMIP5 emerges later than in the CESM1-LE, we next evaluate how the internal variability and forced trends in longwave radiation differ between the CESM1-LE and the CESM2-CMIP5 (Fig. 15). Surface upwelling longwave radiation trends in the CESM2-CMIP5 are less than in the CESM1-LE during the fall, indicating a slower rate of surface warming. This slower rate of surface change translates to smaller OLR trends, delaying OLR emergence. In the summer, however, OLR increases are comparable between the CESM1-LE and the CESM2-CMIP5 despite larger surface warming in the CESM1-LE. This seasonal difference between radiation fields suggests that more opaque summer clouds and atmosphere in the CESM2-CMIP5 than the CESM1-LE prevent differences in surface warming from influencing the TOA longwave radiation budget.

Having compared forced trends in longwave radiation between the CESM1-LE and the CESM2-CMIP5, we now compare the net internal climate variability (Fig. 15b). Surface longwave radiation variability in the CESM2-CMIP5 is greater than in the CESM1-LE from November through April, but less than in the CESM1-LE from June through September. Despite these differences in variability at the surface, however, OLR variability in the CESM1-LE and the CESM2-CMIP5 is very similar at the TOA. Collectively, comparing forced trends and variability between the CESM1-LE and the CESM2-CMIP5 indicates that more rapid fall surface warming in the CESM1-LE drives the differences in OLR emergence at the top of the atmosphere. Surface longwave radiation in the CESM2-CMIP5 has different variability than the CESM1-LE, but TOA differences in OLR variability are small.

The CESM2-CMIP5 emerges later than the CESM1-LE because it warms less in the fall, but why does this occur? We answer this question by comparing the total shortwave radiation absorbed during the melt season (March–September) with longwave radiation emitted during the Arctic fall (August–November) (Fig. 16). Consistent with the seasonal transfer of energy from summer to fall, longwave radiation emitted during the fall strongly resembles the shortwave energy absorbed during the summer. In other words, the CESM2-CMIP5 absorbs shortwave radiation more slowly than the CESM1-LE, causing it to emit less longwave radiation during the fall and emerge later.

To confirm that differences in shortwave absorption are responsible for fall OLR differences, we additionally determine the time to emergence of TOA absorbed shortwave radiation. We present these results for individual months during the melt season (March–September) as well as for the annual mean in Fig. 17. Our results show that the time to emergence of Arctic absorbed shortwave radiation precedes that of outgoing longwave radiation (Fig. 6) by nearly 5 years in the annual average, and by two decades for individual months. That said, both shortwave and longwave radiation share that they emerge latest in spring and earliest in late summer and early fall. Also consistent with our outgoing longwave radiation results, fall Arctic absorbed shortwave radiation emerges later in the CESM2-CMIP5 than the CESM1-LE (Fig. 17b). Collectively, comparing the time to emergence of OLR and absorbed shortwave radiation supports our conclusion that clouds and sea ice mediate the emergence of fall OLR by modifying the shortwave energy budget during the melt season.

4. Discussion

When will changes in Arctic longwave radiation emerge from internal variability? Why do some months emerge earlier than others? We have investigated these questions by expanding the standard signal-to-noise framework of climate signal emergence to comprehensively consider internal climate variability in future changes. One of the most important results we find is that the predicted time to emergence of Arctic OLR varies by month. Specifically, the mean time to emergence in September (22 years) precedes April (42 years) by two decades. Observed OLR changes from the CERES record (2001–21) largely remain within the CESM1-LE's estimate of internal climate variability. The probability of emergence for fall months and the annual average, however, surpasses 50% by 2025. With spring emergence predicted decades later, our results underscore the necessity of a seamless energy budget record extending into the mid-twenty-first century. Upcoming radiation budget continuity missions (e.g., NASA's Libera) will be critical for the future detection and attribution of Arctic climate change.

A further novelty of this work is that we identify how surface and atmospheric climate processes influence OLR time to emergence by comparing radiation fields. We find that monthly differences in emergence are driven by differences in surface warming and internal variability. Monthly differences in surface warming are linked to the well-studied processes of sea ice–albedo feedback and seasonal energy transfer (e.g., Serreze and Barry 2011). Monthly differences in OLR internal variability are linked to the seasonally changing heat capacity of the Arctic surface as well as the opacity of the
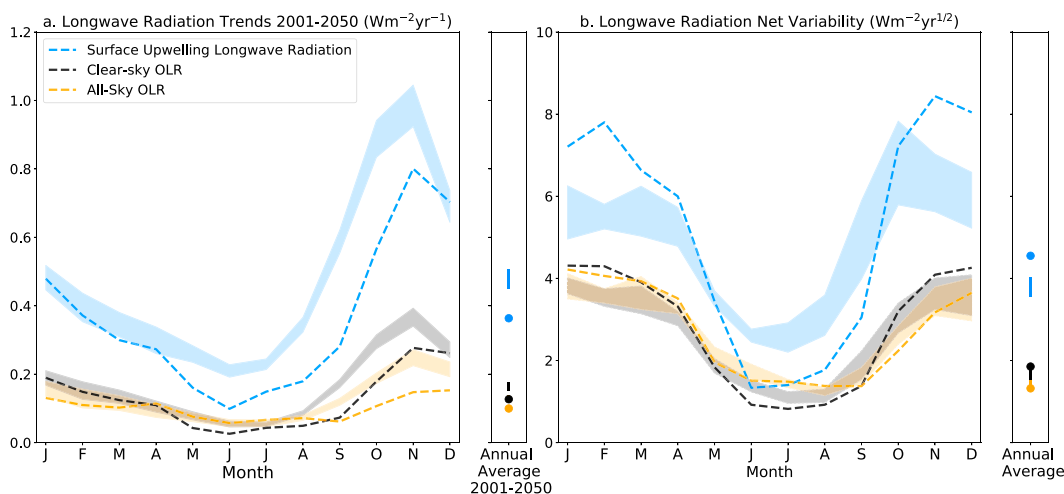
FIG. 15. Comparison of longwave radiation changes and variability between the CESM1-LE and the CESM2-CMIP5. (a) Mean longwave radiations trends from 2001 to 2050. Surface upwelling longwave radiation (blue), TOA clear-sky outgoing longwave radiation (black), and TOA all-sky outgoing longwave radiation (yellow). Dashed lines show values from the CESM2-CMIP5 and shaded regions show a 95% confidence interval from the CESM1-LE. (b) Net variability of longwave radiation from preindustrial control simulations. Colors are as in (a).

atmosphere and clouds. The atmosphere and clouds delay emergence most in the winter and spring. Minimal coupling between the surface and atmosphere during this time likely prevents surface changes from being observed from space. Our results suggest that accurately predicting the future Arctic energy budget requires a realistic representation of all of these processes in climate models.

Comparing the CESM1-LE and CESM2-CMIP5 ensembles reveals how Arctic clouds and sea ice influence OLR emergence. With fewer optically thick, liquid-containing clouds, the shortwave energy budget in the CESM1-LE is more sensitive to sea ice loss than the CESM2-CMIP5, leading to faster energy uptake and more rapid fall warming. The mean state of Arctic

sea ice also contributes to differences between model versions: the CESM1-LE starts with greater sea ice coverage than CESM2 and loses that sea ice more rapidly (Holland et al. 2023, manuscript submitted to *Geosci. Model Dev.*). These results indicate that the shortwave radiation budget during the critical melt season has an outsized role in determining the emergence of fall OLR. Fall sea ice and cloud states are less important than the uptake of solar radiation during the summer. As a whole, these results demonstrate that the time to emergence of fall OLR changes depends largely on the representation of summer sea ice and clouds. Consequently, the large monthly differences between spring and fall OLR time to emergence also depend on summer sea ice and clouds.
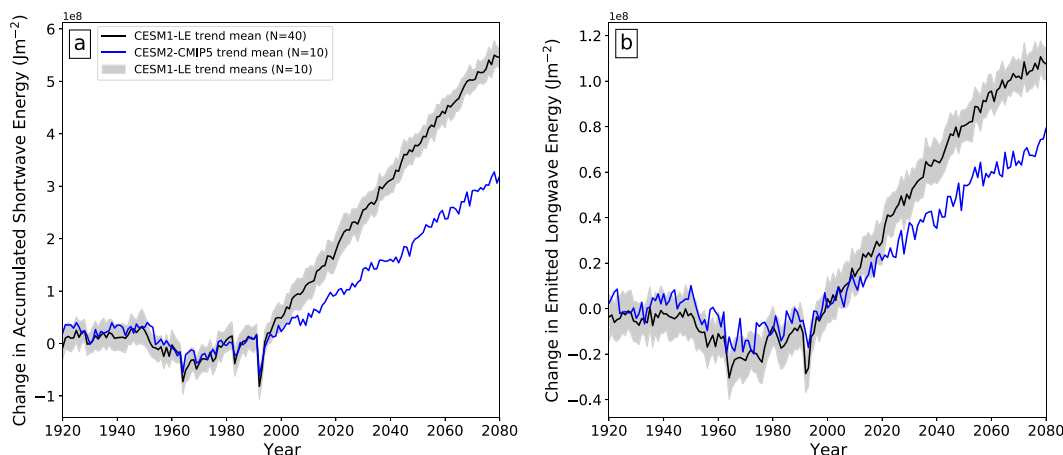

FIG. 16. Change in absorbed shortwave and emitted longwave radiation in the CESM1-LE and the CESM2-CMIP5. (a) Change in shortwave radiation absorbed over the melt season (March–September) relative to preindustrial control. (b) Change in longwave radiation emitted over the fall (August–November) relative to preindustrial control. Bootstrapping is used analogously to Fig. 14 to compare ensembles of different sizes.
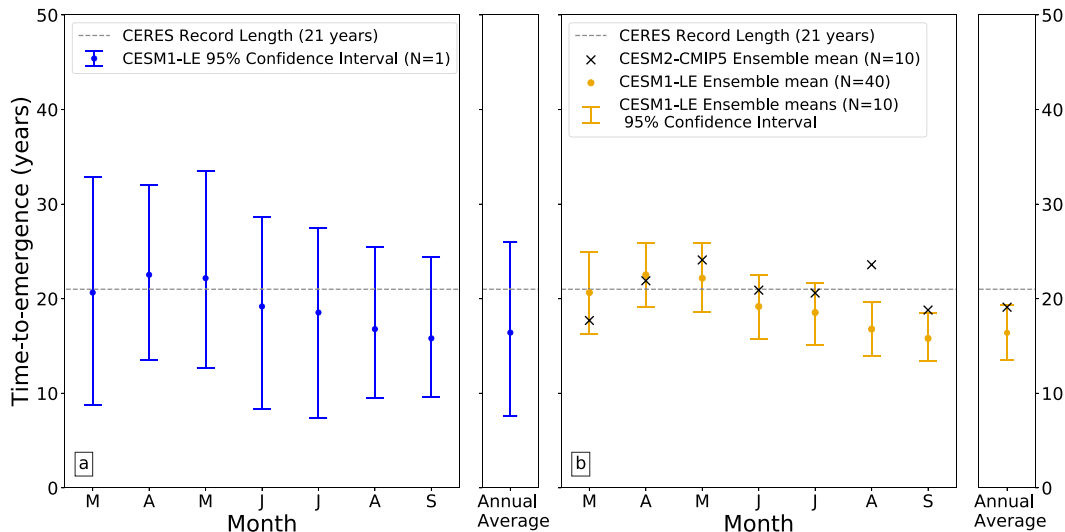
FIG. 17. Monthly and annual time to emergence of top-of-atmosphere all-sky Arctic absorbed shortwave radiation. (a) Average time to emergence and uncertainty in the CESM1-LE. Blue error bars span a bootstrapped 95% confidence interval on time to emergence for individual ($N = 1$) ensemble members, (b) Time to emergence in the CESM1-LE and CESM2-CMIP5 ensembles. Yellow error bars indicate a bootstrapped 95% confidence interval on 10-member ensembles from the CESM1-LE. In both panels the dashed gray line indicates the current length of the CERES observational record.

In addition to studying monthly differences in time to emergence, we also examined the emergence of changes in annually averaged OLR. Annually averaged OLR changes (Fig. 6) emerge before all individual months, despite being by definition their average. While the annual mean OLR trend is indeed the average of trends for individual months (Fig. 5), the annual mean internal variability is reduced relative to the mean of individual months (Fig. 8), accelerating emergence. Annually averaged OLR would likely emerge even earlier relative to individual months in regions other than the Arctic, where seasonal contrasts are less extreme.

Emergence studies using a single model large ensemble have distinct advantages and disadvantages compared to studies using few ensemble members across multiple models. Single-model large ensembles can isolate the role of internal variability but ignore uncertainty in model physics. Multimodel studies account for both internal climate variability and model physics but cannot separate their relative importance. We address the former shortcoming by using a model that has been extensively validated in the Arctic. To address the latter, multimodel studies often use synthetic ensembles to estimate the role of internal climate variability alone (e.g., Chepfer et al. 2018; Sledd and L'Ecuyer 2021a). A synthetic ensemble estimates both variability and forcing from a single simulation, and then creates "synthetic" time series with these estimated properties. To evaluate the synthetic ensemble approach, we generate a synthetic ensemble of annually averaged OLR time series from each member of the CESM1-LE following the methods of Chepfer et al. (2018) and Sledd and L'Ecuyer (2021a). We find that only a single synthetic ensemble produces a time-to-emergence distribution that is indistinguishable from the large ensemble's "true" distribution (Fig. S5c).

The remaining synthetic ensembles uniformly underestimate both the mean and standard deviation of OLR emergence (Figs. S5a,b). This result suggests that a large ensemble may be needed to sample the full range of internal climate variability in the Arctic.

By studying climate signal emergence using model fields free from measurement uncertainty, our results represent a lower limit on time to emergence. Accounting for observational uncertainty will delay the predicted time to emergence, but by how long is yet to be studied. Quantifying this delay requires not only estimates of instrument uncertainty and satellite drift, but also knowledge of the underlying correlation structure of the gridded observations used to compute Arctic time series. Furthermore, methods accounting for observational uncertainty within the signal-to-noise framework (Leroy et al. 2008) do not consider observational records that combine multiple instruments over various time scales, such as CERES.

While we have used the CERES record here, broadband radiation is not the only multidecadal satellite record of Arctic change. Multidecadal spectral OLR records (e.g., from NASA's Atmospheric Infrared Sounder) provide further insight into OLR changes. Specifically, spectral radiation is more easily traced to the climate processes driving emergence than broadband radiation (e.g., Huang 2013; Peterson et al. 2019). Unfortunately, the modeled spectral OLR needed to estimate the background of internal variability and project future change is rarely produced by models. If spectral model fields were available, however, the methods developed here could be applied to identify the spectral drivers of emergence and expose compensating biases hidden in broadband OLR. Easy-to-use and computationally affordable tools for producing

spectral OLR will open new doors for studies of climate change attribution and climate model evaluation.

5. Conclusions

This study investigates the influence of seasonal Arctic climate processes on the emergence of Arctic outgoing longwave radiation (OLR). We combined satellite observations and climate model large ensemble data to evaluate OLR emergence, compared monthly emergence differences, and traced those differences to specific Arctic climate processes. The major conclusions of this work are:

1) September is the earliest month to emerge (mean emergence of 22 years for observations beginning in 2001), while April is the latest month to emerge (mean emergence of 42 years for observations beginning in 2001). This difference is due in roughly equal parts to lower internal variability in September compared to April and greater forced change in September compared to April.

2) Internal variability leads to a wide range of possible OLR emergence times. The 95% confidence interval on September OLR emergence spans 19 years from 2014 to 2032 while the 95% confidence interval on April OLR emergence spans 40 years from 2023 to 2062.

3) Surface changes control the seasonal behavior of OLR emergence. The Arctic atmosphere and clouds delay emergence more in the winter and spring than in the fall, increasing the monthly differences set by surface changes.

4) Forced changes in sea ice concentration, surface temperature, and broadband top-of-atmosphere radiation resemble the observed trends, demonstrating the human fingerprint on Arctic climate change.

5) Differences between preindustrial and twenty-first-century OLR variability do not modify predictions of OLR emergence. OLR variability becomes statistically different from preindustrial variability during the twenty-first century, but this change in variability occurs too late to modify the trends that determine emergence.

6) The accurate representation of clouds and sea ice has a large impact on fall OLR time to emergence. Specifically, larger preindustrial sea ice extent and a less opaque atmosphere during the melt season causes more fall warming and earlier emergence.

REFERENCES

Barnhart, K. R., C. R. Miller, I. Overeem, and J. E. Kay, 2016: Mapping the future expansion of Arctic open water. *Nat. Climate Change*, **6**, 280–285, https://doi.org/10.1038/nclimate2848.

Boisvert, L. N., and J. C. Stroeve, 2015: The Arctic is becoming warmer and wetter as revealed by the atmospheric infrared sounder. *Geophys. Res. Lett.*, **42**, 4439–4446, https://doi.org/10.1002/2015GL063775.

Chepfer, H., V. Noel, M. Chiriaco, B. Wielicki, D. Winker, N. Loeb, and R. Wood, 2018: The potential of a multidecade spaceborne lidar record to constrain cloud feedback. *J. Geophys. Res. Atmos.*, **123**, 5433–5454, https://doi.org/10.1002/2017JD027742.

Chylek, P., C. Folland, J. D. Klett, M. Wang, N. Hengartner, G. Lesins, and M. K. Dubey, 2022: Annual mean Arctic amplification 1970–2020: Observed and simulated by CMIP6 climate models. *Geophys. Res. Lett.*, **49**, e2022GL099371, https://doi.org/10.1029/2022GL099371.

Danabasoglu, G., and Coauthors, 2020: The Community Earth System Model version 2 (CESM2). *J. Adv. Model. Earth Syst.*, **12**, e2019MS001916, https://doi.org/10.1029/2019MS001916.

DeRepentigny, P., A. Jahn, M. M. Holland, and A. Smith, 2020: Arctic Sea ice in two configurations of the CESM2 during the 20th and 21st centuries. *J. Geophys. Res. Oceans*, **125**, e2020JC016133, https://doi.org/10.1029/2020JC016133.

Deser, C., and Coauthors, 2020: Insights from Earth system model initial-condition large ensembles and future prospects. *Nat. Climate Change*, **10**, 277–286, https://doi.org/10.1038/s41558-020-0731-2.

Ding, Q., and Coauthors, 2018: Fingerprints of internal drivers of Arctic Sea ice loss in observations and model simulations. *Nat. Geosci.*, **12**, 28–33, https://doi.org/10.1038/s41561-018-0256-8.

England, M. R., I. Eisenman, N. J. Lutsko, and T. J. W. Wagner, 2021: The recent emergence of Arctic amplification. *Geophys. Res. Lett.*, **48**, e2021GL094086, https://doi.org/10.1029/2021GL094086.

English, J. M., J. E. Kay, A. Gettelman, X. Liu, Y. Wang, Y. Zhang, and H. Chepfer, 2014: Contributions of clouds, surface albedos, and mixed-phase ice nucleation schemes to Arctic radiation biases in CAM5. *J. Climate*, **27**, 5174–5197, https://doi.org/10.1175/JCLI-D-13-00608.1.

Eyring, V., and Coauthors, 2021: Human influence on the climate system. *Climate Change 2021: The Physical Science Basis*,

V. Masson-Delmotte et al., Eds., Cambridge University Press, 423–552, https://doi.org/10.1017/9781009157896.005.

Fasullo, J. T., J.-F. Lamarque, C. Hannay, N. Rosenbloom, S. Tilmes, P. DeRepentigny, A. Jahn, and C. Deser, 2022: Spurious late historical-era warming in CESM2 driven by prescribed biomass burning emissions. *Geophys. Res. Lett.*, **49**, e2021GL097420, https://doi.org/10.1029/2021GL097420.

Feldman, D. R., C. A. Algieri, W. D. Collins, Y. L. Roberts, and P. A. Pilewskie, 2011: Simulation studies for the detection of changes in broadband albedo and shortwave nadir reflectance spectra under a climate change scenario. *J. Geophys. Res.*, **116**, D24103, https://doi.org/10.1029/2011JD016407.

Forster, P., and Coauthors, 2021: The Earth's energy budget, climate feedbacks, and climate sensitivity. *Climate Change 2021:The Physical Science Basis*, V. Masson-Delmotte et al., Eds., Cambridge University Press, 923–1054, https://doi.org/10.1017/9781009157896.009.

Fyfe, J. C., K. von Salzen, N. P. Gillett, V. K. Arora, G. M. Flato, and J. R. McConnell, 2013: One hundred years of Arctic surface temperature variation due to anthropogenic influence. *Sci. Rep.*, **3**, 2645, https://doi.org/10.1038/srep02645.

Gillett, N. P., D. A. Stone, P. A. Stott, T. Nozawa, A. Y. Karpechko, G. C. Hegerl, M. F. Wehner, and P. D. Jones, 2008: Attribution of polar warming to human influence. *Nat. Geosci.*, **1**, 750–754, https://doi.org/10.1038/ngeo338.

Huang, Y., 2013: A simulated climatology of spectrally decomposed atmospheric infrared radiation. *J. Climate*, **26**, 1702–1715, https://doi.org/10.1175/JCLI-D-12-00438.1.

Hurrell, J. W., and Coauthors, 2013: The Community Earth System Model: A framework for collaborative research. *Bull. Amer. Meteor. Soc.*, **94**, 1339–1360, https://doi.org/10.1175/BAMS-D-12-00121.1.

Jahn, A., 2018: Reduced probability of ice-free summers for 1.5°C compared to 2°C warming. *Nat. Climate Change*, **8**, 409–413, https://doi.org/10.1038/s41558-018-0127-8.

——, J. E. Kay, M. M. Holland, and D. M. Hall, 2016: How predictable is the timing of a summer ice-free Arctic? *Geophys. Res. Lett.*, **43**, 9113–9120, https://doi.org/10.1002/2016GL070067.

Kay, J. E., M. M. Holland, and A. Jahn, 2011: Inter-annual to multi-decadal Arctic Sea ice extent trends in a warming world. *Geophys. Res. Lett.*, **38**, L15708, https://doi.org/10.1029/2011GL048008.

——, and Coauthors, 2015: The Community Earth System Model (CESM) large ensemble project: A community resource for studying climate change in the presence of internal climate variability. *Bull. Amer. Meteor. Soc.*, **96**, 1333–1349, https://doi.org/10.1175/BAMS-D-13-00255.1.

——, L. Bourdages, N. B. Miller, A. Morrison, V. Yettella, H. Chepfer, and B. Eaton, 2016: Evaluating and improving cloud phase in the Community Atmosphere Model version 5 using spaceborne lidar observations. *J. Geophys. Res. Atmos.*, **121**, 4162–4176, https://doi.org/10.1002/2015JD024699.

——, and Coauthors, 2022: Less surface sea ice melt in the CESM2 improves Arctic sea ice simulation with minimal non-polar climate impacts. *J. Adv. Model. Earth Syst.*, **14**, e2021MS002679, https://doi.org/10.1029/2021MS002679.

Kirchmeier-Young, M. C., F. W. Zwiers, and N. P. Gillett, 2017: Attribution of extreme events in Arctic sea ice extent. *J. Climate*, **30**, 553–571, https://doi.org/10.1175/JCLI-D-16-0412.1.

Knutson, T., J. Kossin, C. Mears, J. Perlwitz, and M. Wehner, 2017: Detection and attribution of climate change. *Climate Science Special Report: Fourth National Climate Assessment*,

D. J. Wuebbles et al., Eds., U.S. Global Change Research Program, 114–132, https://doi.org/10.7930/J01834ND.

Landrum, L., and M. M. Holland, 2020: Extremes become routine in an emerging new Arctic. *Nat. Climate Change*, **10**, 1108–1115, https://doi.org/10.1038/s41558-020-0892-z.

Leroy, S. S., J. G. Anderson, and G. Ohring, 2008: Climate signal detection times and constraints on climate benchmark accuracy requirements. *J. Climate*, **21**, 841–846, https://doi.org/10.1175/2007JCLI1946.1.

Loeb, N. G., and Coauthors, 2018: Clouds and the Earth's Radiant Energy System (CERES) Energy Balanced and Filled (EBAF) Top-of-Atmosphere (TOA) edition-4.0 data product. *J. Climate*, **31**, 895–918, https://doi.org/10.1175/JCLI-D-17-0208.1.

Manabe, S., and R. J. Stouffer, 1980: Sensitivity of a global climate model to an increase of CO_2 concentration in the atmosphere. *J. Geophys. Res.*, **85**, 5529–5554, https://doi.org/10.1029/JC085iC10p05529.

McIlhattan, E. A., J. E. Kay, and T. S. L'Ecuyer, 2020: Arctic clouds and precipitation in the Community Earth System Model version 2. *J. Geophys. Res. Atmos.*, **125**, e2020JD032521, https://doi.org/10.1029/2020JD032521.

Meier, W. N., F. Fetterer, A. K. Windagel, and J. S. Stewart, 2021: NOAA/NSIDC climate data record of passive microwave sea ice concentration, version 4. National Snow and Ice Data Center, accessed 19 July 2022, https://doi.org/10.7265/efmz-2t65.

NASA/LARC/SD/ASDC, 2019: CERES Energy Balanced and Filled (EBAF) TOA and surface monthly means data in netCDF edition 4.1. NASA Langley Atmospheric Science Data Center, accessed 19 July 2022, https://doi.org/10.5067/TERRA-AQUA/CERES/EBAF_L3B.004.1.

National Academies of Sciences, Engineering and Medicine, 2016: *Attribution of Extreme Weather Events in the Context of Climate Change*. National Academies Press, 186 pp., https://doi.org/10.17226/21852.

Peterson, C. A., X. Chen, Q. Yue, and X. Huang, 2019: The spectral dimension of Arctic outgoing longwave radiation and greenhouse efficiency trends from 2003 to 2016. *J. Geophys. Res. Atmos.*, **124**, 8467–8480, https://doi.org/10.1029/2019JD030428.

Phojanamongkolkij, N., S. Kato, B. A. Wielicki, P. C. Taylor, and M. G. Mlynczak, 2014: A comparison of climate signal trend detection uncertainty analysis methods. *J. Climate*, **27**, 3363–3376, https://doi.org/10.1175/JCLI-D-13-00400.1.

Raghuraman, S. P., D. Paynter, and V. Ramaswamy, 2021: Anthropogenic forcing and response yield observed positive trend in Earth's energy imbalance. *Nat. Commun.*, **12**, 4577, https://doi.org/10.1038/s41467-021-24544-4.

Rohde, R. A., and Z. Hausfather, 2020: The Berkeley Earth land/ocean temperature record. *Earth Syst. Sci. Data*, **12**, 3469–3479, https://doi.org/10.5194/essd-12-3469-2020.

Screen, J. A., and I. Simmonds, 2010: The central role of diminishing sea ice in recent Arctic temperature amplification. *Nature*, **464**, 1334–1337, https://doi.org/10.1038/nature09051.

Serreze, M. C., and R. G. Barry, 2011: Processes and impacts of Arctic amplification: A research synthesis. *Global Planet. Change*, **77**, 85–96, https://doi.org/10.1016/j.gloplacha.2011.03.004.

——, A. P. Barrett, J. C. Stroeve, D. N. Kindig, and M. M. Holland, 2009: The emergence of surface-based Arctic amplification. *Cryosphere*, **3**, 11–19, https://doi.org/10.5194/tc-3-11-2009.

Sledd, A., and T. S. L'Ecuyer, 2021a: Uncertainty in forced and natural Arctic solar absorption variations in CMIP6 models. *J. Climate*, **34**, 931–948, https://doi.org/10.1175/JCLI-D-20-0244.1.

——, and ——, 2021b: Emerging trends in Arctic solar absorption. *Geophys. Res. Lett.*, **48**, e2021GL095813, https://doi.org/10.1029/2021GL095813.

Taylor, P. C., and Coauthors, 2022: Process drivers, inter-model spread, and the path forward: A review of amplified Arctic warming. *Front. Earth Sci.*, **9**, 758361, https://doi.org/10.3389/feart.2021.758361.

Tiao, G. C., and Coauthors, 1990: Effects of autocorrelation and temporal sampling schemes on estimates of trend and spatial correlation. *J. Geophys. Res.*, **95**, 20 507–20 517, https://doi.org/10.1029/JD095iD12p20507.

Weatherhead, E. C., and Coauthors, 1998: Factors affecting the detection of trends: Statistical considerations and applications to environmental data. *J. Geophys. Res.*, **103**, 17 149–17 161, https://doi.org/10.1029/98JD00995.

Wielicki, B. A., and Coauthors, 2013: Achieving climate change absolute accuracy in orbit. *Bull. Amer. Meteor. Soc.*, **94**, 1519–1539, https://doi.org/10.1175/BAMS-D-12-00149.1.

Wyburn-Powell, C., A. Jahn, and M. R. England, 2022: Modeled interannual variability of Arctic sea ice cover is within observational uncertainty. *J. Climate*, **35**, 6827–6842, https://doi.org/10.1175/JCLI-D-21-0958.1.